nature water

Article

https://doi.org/10.1038/s44221-024-00362-y

A highly selective and energy efficient approach to boron removal overcomes the Achilles heel of seawater desalination

Received: 2 May 2024

Accepted: 19 November 2024

Published online: 20 January 2025

Check for updates

Weiyi Pan[1,4,5], Debashis Roy[2,5], Betül Uralcan[1,3], Sohum K. Patel[1], Arpita Iddya[1], Eungjin Ahn[2], Amir Haji-Akbari[1], Jovan Kamcev[2] ✉ & Menachem Elimelech[1,4] ✉

Selective removal of trace contaminants from water remains a crucial challenge in water treatment. Boron is a trace contaminant that is ubiquitous in seawater and has been widely detected in groundwater. Current boron removal methods, such as multi-stage reverse osmosis and ion-exchange adsorption, are chemical and energy intensive, necessitating the development of more sustainable technologies. Here we address this challenge by developing surface functionalized microporous electrodes that enable boron-selective bipolar membrane-assisted electrosorption. Our study demonstrates that micropore functionalization with oxygen-containing (hydroxyl, lactone and carboxyl) and boron-selective (dopamine, 3-methylamino-1,2-propanediol and *N*-methyl-D-glucamine) functional groups substantially improves electrode performance for boron removal and selectivity. The functionalized electrodes exhibit a boron removal selectivity that is an order of magnitude higher than that of the pristine electrode, facilitating energy efficient boron electrosorption. We identify hydroxyl groups as the key factor in enhancing boron removal performance and selectivity during electrosorption. Molecular dynamics simulations demonstrate the underlying mechanisms of boron selectivity, highlighting the role of hydrogen bonding between hydroxyl groups and boron in governing the boron-selective electrosorption process.

Over one billion people worldwide lack access to clean water[1]. The escalating water shortage, exacerbated by climate change and rapid population growth[2], poses a major hurdle to sustainable development. To address this challenge, unconventional water sources, such as seawater and brackish water, have gained heightened attention as a means to augment water supply[3]. However, these water sources often contain high concentrations of inorganic salts and harmful trace contaminants, such as boron, arsenic and per- and polyfluoroalkyl substances[4]. Whereas these sources hold potential to alleviate water scarcity, implementing sustainable and cost-effective solutions remains a formidable task[5,6]. Currently, reverse osmosis (RO) stands as the dominant desalination technology[7], offering efficient water–salt separation[8], low energy consumption[9] and small footprint. Despite its advantages, certain contaminants, such as boron, cannot be efficiently removed through single-pass RO and necessitate additional treatment to meet drinking water and agriculture water standards[10].

[1]Department of Chemical and Environmental Engineering, Yale University, New Haven, CT, USA. [2]Department of Chemical Engineering, University of Michigan, Ann Arbor, MI, USA. [3]Department of Chemical Engineering, Boğaziçi University, Istanbul, Turkey. [4]Present address: Department of Civil and Environmental Engineering, Rice University, Houston, TX, USA. [5]These authors contributed equally: Weiyi Pan, Debashis Roy. ✉e-mail: jkamcev@umich.edu; menachem.elimelech@yale.edu

Boron is ubiquitous in seawater at a concentration range of 4–6 mg l^{-1} (ref. 11). The World Health Organization[12], the European Union[13] and Health Canada[14] have established health-based limits for boron in drinking water, ranging from 1 to 2.4 mg l^{-1}. Certain states in the United States (for example, California and Florida) have established drinking water standards for boron, ranging from 0.6 to 1 mg l^{-1} (ref. 15). Removing trace levels of boron from aqueous solutions presents a considerable challenge, resulting in only a few effective separation methods to date, such as multi-pass high pH RO and boron-selective adsorption[10,16,17]. However, the use of multi-pass RO involves inherent pH swings and requires substantial chemical dosing[16], which is economically and environmentally unsustainable. The additional RO passes also increase the overall energy consumption of the seawater desalination process (10–15%)[18], leading to increased costs[19]. Boron-selective ion-exchange resins offer an alternative to multi-pass RO, but their relatively slow removal kinetics necessitate large and costly bed volumes[16,20]. Moreover, the regeneration of these resins involves the use of large quantities of strong acids and bases, thereby incurring substantial financial and environmental costs[19]. The major shortcomings of both multi-pass RO and boron-selective sorbents highlight the pressing need for an improved and sustainable boron removal technology.

Electrosorption presents a promising solution to address the challenge of efficient boron removal. In electric double-layer-based electrosorption, also known as capacitive deionization, a small electric potential (<1.4 V) is applied across a pair of porous, carbon-based electrodes[21,22]. The applied voltage prompts ions in the solution to migrate towards the oppositely charged electrode, where they are captured and stored in the electrical double layers within the electrode micropores. Leveraging the exceptionally high surface areas of porous carbon materials[23], a large number of ions can be extracted from the solution before electrode saturation occurs. Upon removing or reversing the electric potential, the captured ions are released from the micropores to form a brine solution, thus regenerating the electrosorption sites on the electrode. Electrosorption exhibits optimal energy efficiency for low salinity waters and moderate extents of ion removal[24,25], making it a particularly suitable and energetically favourable method for trace boron removal, such as from seawater RO permeate.

Leveraging electrosorption for boron removal entails addressing two key challenges. First, boron's pK_a of 9.24 indicates that most (>90%) of boron exists in the form of boric acid, $B(OH)_3$, in seawater (pH 8.1). Various strategies have been explored to elevate the pH at the anode side[11,26–28], facilitating the conversion of boric acid to borate, $B(OH)_4^-$, for electrosorption. One approach involves the use of a flow-through electrosorption cell with carbon electrodes, creating a high pH environment at the anode side through the Faradaic reaction at the cathode electrode, where hydroxide generated during oxygen reduction migrates to the anode side[26,27]. A recent study employed an asymmetric flow-by electrosorption system, incorporating a carbon cloth anode and a graphite cathode separated by an anion exchange membrane, with the graphite cathode facilitating pH increase by water reduction[28]. More recently, we introduced a bipolar membrane-assisted electrosorption device that effectively dissociates water and releases hydroxide to the anode side, thus increasing pH at that side[11]. This electrified, chemical-free process is superior to flow-through electrosorption in terms of boron removal capacity and energy consumption.

Another key challenge in electrosorption is achieving selectivity for boron over competing anions, particularly chloride[28]. Higher boron selectivity implies a lower energy consumption to remove the same amount of boron, making this process competitive with current industrial practices (for example, multi-pass RO and ion-exchange adsorption). Electrosorption, however, exhibits limited effectiveness in achieving boron selectivity. A recent review concludes that electrode functionalization with specific functional groups shows the most promise for enhancing selectivity in electrosorption[29]. Boron is known to form complexes with vicinal diol groups (that is, two hydroxyl groups attached to adjacent atoms)[30]. Recent studies explored the development of adsorptive materials containing such functional groups, namely *N*-methyl-D-glucamine and dopamine-modified materials, for selective boron adsorption[31–33]. However, the applicability of this mechanism to electrosorption within electrode micropores remains uncertain due to challenges such as the strong binding between boron and these functional groups, which reduces the reversibility of the electrosorption process. Additionally, the presence of bulky boron-selective functional groups may obstruct pores and hinder boron electrosorption within the micropores of the electrode. These knowledge gaps call for the establishment of fundamental principles for the design of boron-selective electrosorption.

In this study, we explore boron-selective electrosorption employing functionalized carbon cloth anodes for the selective removal of boron from water. Two distinct chemical functionalization methods—basic oxygen-containing groups (hydroxyl, lactone and carboxyl groups) and boron-selective groups (3-methylamino-1,2-propanediol (MAPD), *N*-methyl-D-glucamine (NMDG) and dopamine (DP))—were employed for electrode functionalization. These methods functionalize the electrode micropores, which is critical for selective electrosorption[21,22,29]. We evaluated the boron removal efficiency, selectivity (that is, boron versus chloride) and energy consumption of the functionalized electrodes using a custom-built bipolar membrane-assisted electrosorption cell. Our analysis revealed the relationships between boron selectivity and physico-chemical properties of the electrodes. Finally, we used molecular dynamics simulations to extend the mechanistic understanding of how functional groups influence boron selectivity by elucidating the intrinsic interactions between the functional groups and boron.

Functionalization alters electrode morphology and structure

Comprehensive characterization unveils distinct morphological changes to the carbon cloth electrodes following functionalization. Boron-selective carbon electrodes were fabricated using two categories of chemical functionalization (Fig. 1a). In the first category, the pristine carbon cloth was functionalized by thermal annealing (100–300 °C), UV irradiation (10–60 min) and acid treatment (three different acids and durations). The functionalization approach introduced diverse types of basic oxygen-containing groups, including hydroxyl, lactone and carboxyl groups. In the second category, we utilized boron-selective groups (MAPD, NMDG and DP) to functionalize the pristine electrode. Compared to the pristine electrode, all functionalized electrodes show higher mass loss at elevated temperatures during thermogravimetric analysis (Supplementary Fig. 1), indicating successful introduction of functional groups. Field emission scanning electron microscopy images of the pristine electrode show a smooth and rod-like fibre (Fig. 1b and Supplementary Fig. 2). In contrast, all functionalization techniques introduce structural heterogeneity (for example, cracks and holes) to the fibre surface (Fig. 1c–j), which could be potential active sites for electrosorption. For acid treated electrodes, introduction of fracture and groove-like structure on the fibre surface was evident (Fig. 1c–e), implying strong oxidizing effects of the acid treatment[34,35]. The densities of these structural inhomogeneities increase with duration of acid treatment (Supplementary Fig. 3a–i). Thermal treatment of the electrodes introduced numerous uniformly dispersed small pores and fractures (Fig. 1f), with gradually increasing concentrations at higher temperature (Supplementary Fig. 3j–l). Compared with the pristine electrode, UV irradiation functionalizes the fibre surface through the introduction of defects and net-like interconnected patches (Fig. 1g), which grow into a smaller and randomly distributed groove-like structure at longer UV irradiation (Supplementary Fig. 3m–o). Lastly, for all boron-selective groups functionalized electrodes (Fig. 1h–j), the

https://doi.org/10.1038/s44221-024-00362-y

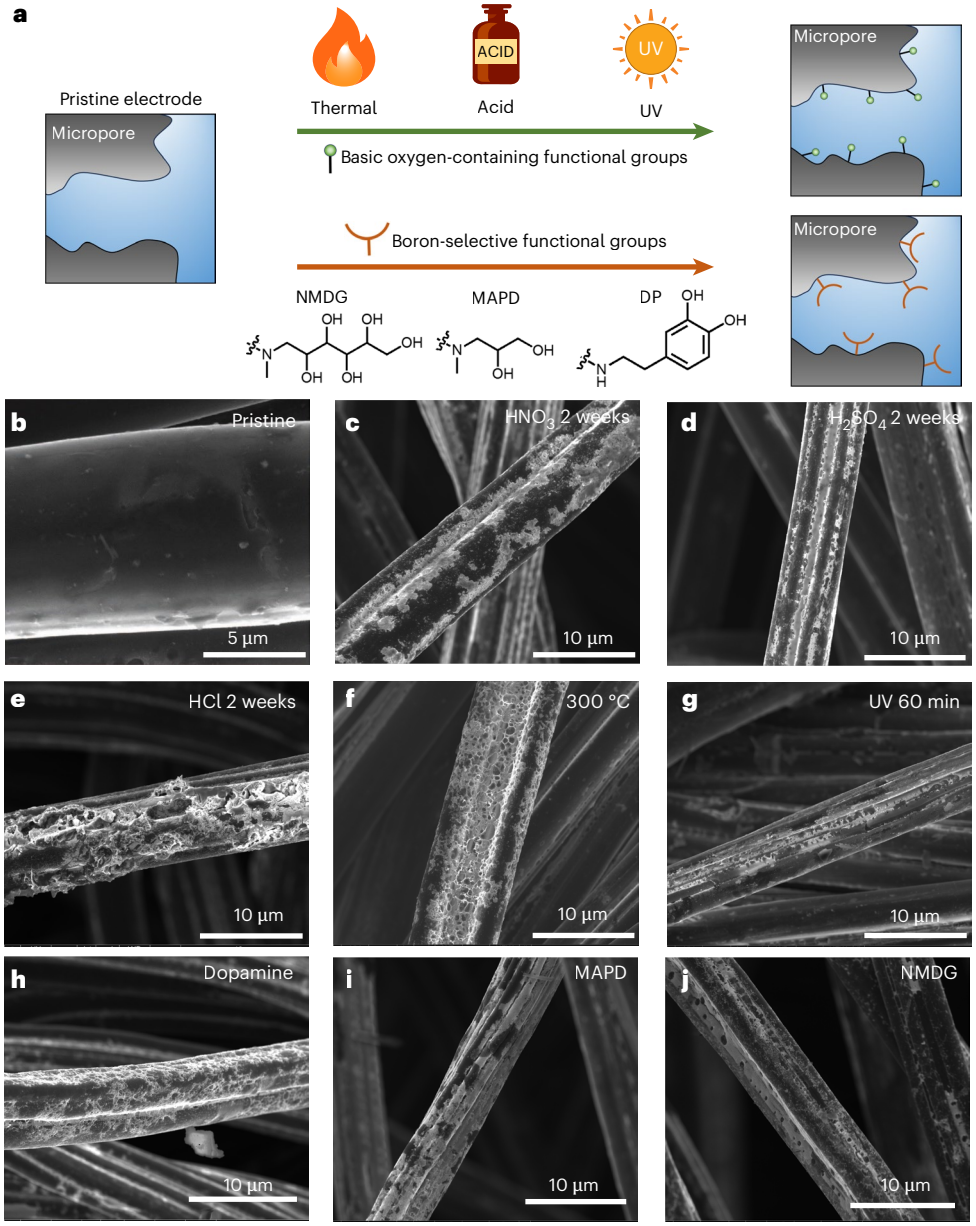

Fig. 1 | Fabrication procedures and morphological changes of functionalized electrodes. a, Illustration of the electrode functionalization methods. **b**, Morphology of the pristine carbon cloth electrode fibres. **c**–**j**, Morphological changes in electrode fibres after the 2-week treatment with 1 M nitric acid (**c**), 1 M sulfuric acid (**d**) and 1 M hydrochloric acid (**e**); after 300 °C annealing (**f**); after 60 min UV irradiation (**g**); and after the introduction of dopamine (**h**), MAPD (**i**) and NMDG (**j**). Commercial carbon cloth served as the base material, undergoing two categories of chemical functionalization to introduce distinct groups: basic oxygen-containing moieties and boron-selective groups. The upper part in **a** demonstrates the introduction of basic oxygen-containing groups via thermal annealing (100–300 °C), acid treatment (1 M nitric acid, 1 M sulfuric acid and 1 M hydrochloric acid for varying treatment durations) and UV irradiation (10–60 min). The lower part of the panel illustrates the introduction of boron-selective groups (DP, MAPD, and NMDG). Representative scanning electron microscopy (SEM) images of the resulting electrodes are shown, with additional SEM images available in Supplementary Figs. 2 and 3. DP, MAPD and NMDG represent dopamine, 3-methylamino-1,2-propanediol and *N*-methyl-D-glucamine, respectively.

presence of patch-like layers was evident, with substantial increase of surface structural heterogeneity and undulations, indicating the successful grafting of the MAPD, NMDG and DP molecules on the electrode surface. Despite the introduction of these structural features, the uniformity of the functional groups' distribution, confirmed by scanning electron microscopy-energy dispersive X-ray spectroscopy analysis (Supplementary Fig. 4), is expected to lead to overall uniform electrochemical activity across the electrode.

To further investigate the structure of the electrodes following functionalization, we determined the average surface area, pore diameter and pore volume of the pristine and functionalized electrodes using BET analysis, involving the N_2 adsorption–desorption isotherm method (Supplementary Table 1). Compared to the pristine electrode, the acid treated, thermally treated and UV irradiated electrodes exhibit an increase in surface area (Fig. 2a–c,d–f, blue circles), average pore size (Supplementary Table 1) and pore volume (Supplementary Table 1). These results agree with the morphological analysis showing substantial number of fractures, cracks and groove-like surface heterogeneities on the fibre surface, which increase the overall porosity of the electrodes. In contrast, for the direct surface functionalized samples with MAPD, NMDG and DP, coverage of the fibre surface with distinct patch-like layers results in lowering of the overall porosity.

https://doi.org/10.1038/s44221-024-00362-y

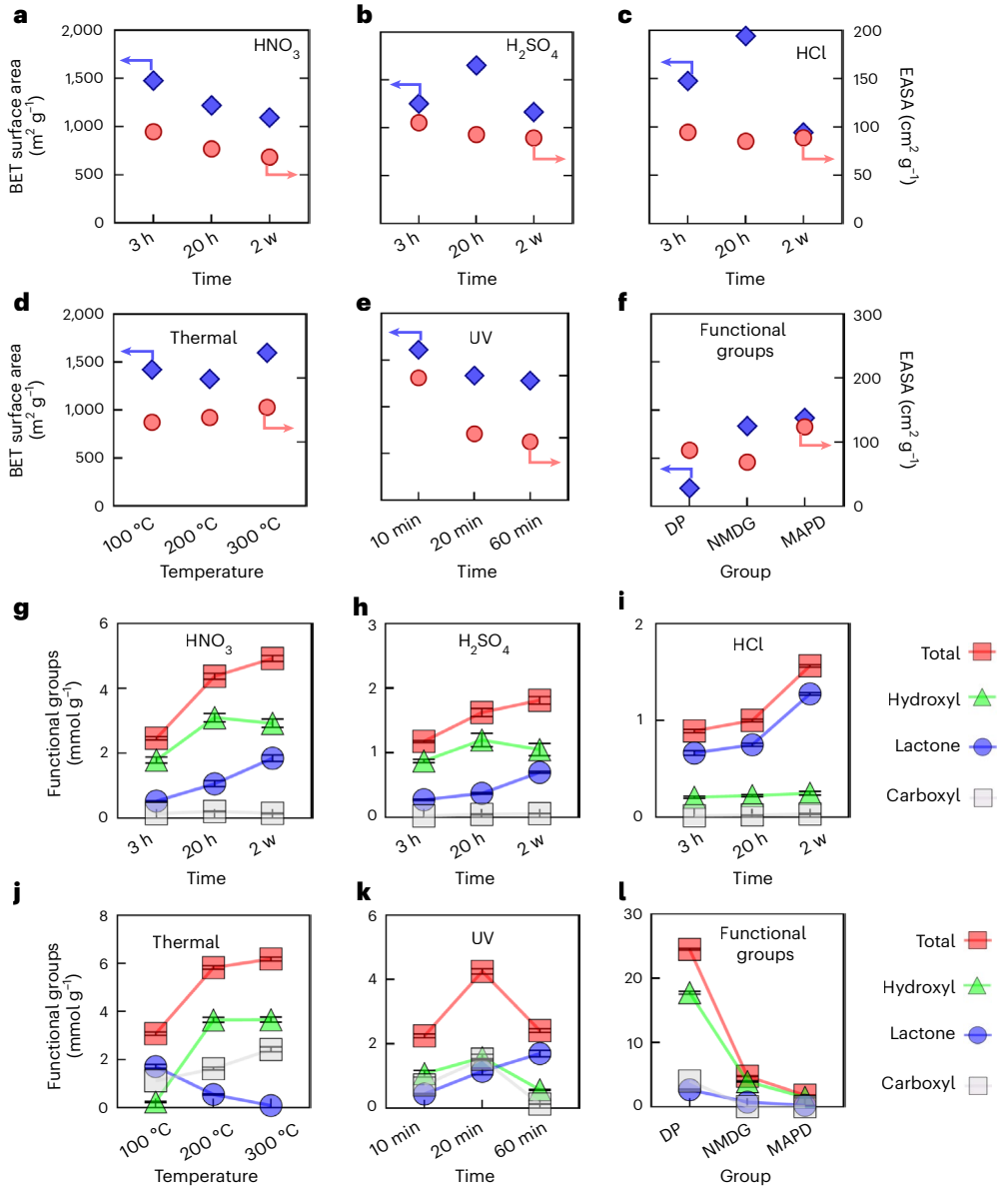

Fig. 2 | Analysis of physico-chemical properties of post functionalized electrodes. a–f, BET surface area (blue circles) and electrochemically active surface area (EASA, pink circles) of electrodes after treatments with 1 M nitric acid (**a**), 1 M sulfuric acid (**b**) and 1 M hydrochloric acid (**c**); after thermal annealing (**d**); after UV irradiation (**e**); and after introductions of boron-selective groups (**f**). **g–l**, Surface functional group concentrations (carboxyl, lactone and hydroxyl groups) determined via Boehm titration of electrodes after treatments with 1 M nitric acid (**g**), 1 M sulfuric acid (**h**) and 1 M hydrochloric acid (**i**); after thermal annealing (**j**); after UV irradiation (**k**); and after introductions of boron-selective groups (**l**). DP, MAPD and NMDG represent dopamine, 3-methylamino-1,2-propanediol and *N*-methyl-D-glucamine, respectively. w represents week. Data in **g–l** are presented as mean ± standard deviation derived from triplicate measurements ($n = 3$).

Notably, the pore size distribution of all functionalized electrodes showed no noteworthy changes (Supplementary Fig. 5).

Another important property of functionalized electrodes is the electrochemically active surface area (EASA). Unlike BET surface area, EASA represents the area of the electrode material that is accessible to the electrolyte for charge transfer and/or storage[36]. To determine the total EASA, cyclic voltammetry at different scan rates was performed for each functionalized electrode to calculate the electrochemical double-layer capacitance (Supplementary Figs. 6–8), following the method discussed by Trasatti and Petrii[37]. The functionalized electrodes exhibit a decreased EASA compared to the pristine electrode (Fig. 2a–f, pink circles). We attribute this decrease to the formation of ultramicropores (diameter < 0.7 nm) and changes in pore structure during the functionalization process, resulting in some surface areas becoming inaccessible to the electrolyte (that is, 0.5 M Na_2SO_4) during EASA measurement, while remaining accessible to N_2 during BET measurement. Notably, the EASA values of electrodes subjected to the same functionalization techniques are comparable.

Functionalization increases surface group density

The concentrations of carboxyl, lactone and hydroxyl functional groups on the pristine and functionalized electrodes were determined via Boehm titration (Fig. 2d–f,j–l). According to the typical pK_a values of carboxyl, hydroxyl and lactone groups on carbonaceous materials, only the carboxyl groups are deprotonated (that is, negatively charged) without applied potential[38]. Relative to the pristine electrode, the concentrations of these functional groups on the surface-modified electrodes were notably higher. Among all the acids used, HNO_3 introduced the highest concentration of basic oxygen-containing groups

(hydroxyl, lactone and carboxyl groups) to the electrode (Fig. 2g), with the 20 h HNO_3-treated electrode sample containing the highest concentration of hydroxyl groups on the surface (3,100 μmol g^{-1}). On the other hand, the HCl and H_2SO_4 oxidation failed to introduce a substantial number of hydroxyl groups (209–250 and 875–1,200 μmol g^{-1} for HCl and H_2SO_4, respectively), probably due to rapid oxidation and subsequent destruction of generated functional groups[39]. Thermal treatment of the electrodes (100–300 °C) introduced a large number of carboxyl (1,118–2,425 μmol g^{-1}), lactone (90–1,715 μmol g^{-1}) and hydroxyl groups (243–3,660 μmol g^{-1}), due to extensive oxidation of the carbon structure in the presence of atmospheric O_2. In contrast, UV exposure oxidized the carbon surface in a more controlled manner. For UV irradiation of a shorter duration (≤20 min), the carbon surface is mostly rich with hydroxyl groups (1,575 μmol g^{-1} for 20 min treated electrode). With a gradual increase of the UV irradiation duration, the concentration of lactone groups increased (1,700 μmol g^{-1} for 60 min treated electrode), which we attribute to cross-linking of the functional moieties forming cyclic aromatic structures[40].

Boron-selective groups were introduced into the microporous structure of the electrode through direct surface grafting. First, the pristine electrodes were irradiated with UV for 30 min to introduce hydroxyl and carboxyl groups on the surface. These partially oxidized electrodes were then treated with thionyl chloride ($SOCl_2$) to introduce acyl chloride (-COCl) groups on the surface. Finally, the NMDG and MAPD molecules were reacted with the -COCl groups on $SOCl_2$-treated electrodes (Supplementary Text 1). The DP was grafted onto the partially oxidized electrode surface by reacting with 1-ethyl-3-(3-dimetylaminopropyl) carbodiimide (Supplementary Text 1). All of these moieties introduce a large number of hydroxyl groups on the surface of the electrodes[31,41]. As expected, the NMDG and MAPD-functionalized electrodes contained a high concentration of hydroxyl groups (3,962 and 1,500 μmol g^{-1} for NMDG and MAPD-functionalized electrodes, respectively), along with low carboxyl concentration (65 and 60 μmol g^{-1} for NMDG and MAPD-functionalized electrodes, respectively), which confirms the successful introduction of the NMDG and MAPD molecules through the novel direct-grafting method. A similar trend was also observed with the DP functionalized electrode, which shows the highest concentrations of hydroxyl (17,750 μmol g^{-1}), lactone (2,700 μmol g^{-1}) and carboxyl (4,050 μmol g^{-1}) groups among all the functionalized electrodes. The surface functional group information obtained from Boehm titration was corroborated by X-ray photoelectron spectroscopy spectra (Supplementary Fig. 9 and Supplementary Table 2).

Functionalized electrodes enhance boron electrosorption

We evaluated the performance of the functionalized electrode with a custom-built bipolar membrane (BPM)-assisted electrosorption set-up (Fig. 3a). The BPM-assisted electrosorption process operates in a flow-by mode with a bipolar membrane separating the anode and cathode chambers (details in Supplementary Fig. 10). The pH profiles of all functionalized electrodes during testing can be found in Supplementary Fig. 11. The pristine electrode exhibited a boron removal capacity (Γ_B) of 1.9 ± 0.1 μmol g^{-1} (Fig. 3b, orange dashed line). Acid treatment, UV irradiation and thermal annealing of the electrodes increased boron removal capacity, ranging from 2.4 ± 0.2 to 5.7 ± 0.5 μmol g^{-1} (Fig. 3b, orange bars). Electrodes modified with functional groups known for high boron selectivity exhibited similar boron removal capacities, ranging from 2.4 ± 0.1 to 4.6 ± 0.1 μmol g^{-1}. At the same time, the electrosorption of chloride ions on the functionalized electrodes decreased (Supplementary Fig. 12). The observed increase in boron removal and decrease in chloride removal is attributed to the elevated functional group densities on the functionalized electrodes, favouring boron over chloride. We note that compared to the pristine electrodes, the overall boron (Fig. 3b) and chloride (Supplementary Fig. 12) electrosorption capacities decrease for the functionalized electrodes, which is consistent with their decreasing EASA values (Fig. 2a–f, pink circles). Because our functionalization methods are versatile and can be applied to other materials, this decrease in the EASA may be overcome by changing the base material (that is, carbon cloth in this study) to other carbonaceous materials with higher EASA.

We subsequently calculated the B/Cl selectivity of the functionalized electrodes based on their boron and chloride removal performances. The pristine electrode showed a B/Cl selectivity of 0.19 ± 0.02 (Fig. 3b, blue dashed line), demonstrating high chloride selectivity over boron. This observation may be due to the higher electrophoretic mobility of chloride ions (-6.98×10^{-4} cm^2 V^{-1} s^{-1}, pH 12.1) compared to borate ions (-2.96×10^{-4} cm^2 V^{-1} s^{-1}, pH 12.1)[42]. The modified electrodes all showed an increase in B/Cl selectivity after functionalization (Fig. 3b, blue squares), suggesting that functional groups govern the boron and chloride electrosorption. The electrode treated with 1 M HNO_3 for 20 h achieved the highest B/Cl selectivity of 2.25 ± 0.06 in all tests. This selectivity is an order of magnitude higher than that of the pristine electrode. Interestingly, electrodes functionalized with the boron-selective groups (DP, NMDG and MAPD) did not exhibit the highest selectivity (1.34 ± 0.22, 1.15 ± 0.06 and 1.13 ± 0.03, respectively). This result suggests that these boron functional groups could form complexes with boron[32], which cannot be efficiently reversed during the discharging stage (that is, 0 V for 40 min)[43].

We further conducted ^{11}B magic angle spinning nuclear magnetic resonance (MAS NMR) with used MAPD-functionalized electrode to investigate the formation of boron-MAPD complexes. We chose the MAPD-functionalized electrode for its high boron removal capacity compared to the NMDG and DP functionalized electrodes. Before analysis, the MAPD-functionalized electrode underwent three charging/discharging cycles in the electrosorption system under the same conditions as the previous experiments. The ^{11}B MAS NMR spectra showed one chemical shift at approximately 3.2 ppm (Fig. 3c). We attribute this chemical shift to monochelate boron-selective functional group (that is, MAPD-borate complexes) based on previous investigations[44,45]. Similar complexes could also form with NMDG and DP functionalized electrodes. This finding suggests that boron-selective functional groups (MAPD, NMDG and DP) form monochelate complexes with boron, which are irreversible under our experimental conditions, compromising the removal capacity and B/Cl selectivity of the corresponding functionalized electrodes.

We also examined the impact of operating parameters on electrode performance and electrode stability. Specifically, we tested the performance of the electrode functionalized with 1 M HNO_3 for 20 h (showing the highest selectivity) under various flow rates (1–6 ml min^{-1}) and applied potentials (1–1.6 V). The results (Supplementary Fig. 13) indicate that whereas boron and chloride removal capacities are highly dependent on operational conditions, B/Cl selectivity remains relatively stable. A 100-cycle (100-h) test using this electrode (that is, 1 M HNO_3 for 20 h) was conducted to demonstrate its longevity (Supplementary Fig. 14). Despite a decline in performance due to Faradaic reactions during the test, the functionalized electrode maintained promising boron removal efficiency and B/Cl selectivity.

Functionalization enables energy efficient electrosorption

We assessed our system performance and benchmarked it against other electrosorption systems using specific energy consumption (SEC) per gram of boron electrosorbed (kWh g-B^{-1}) as the comparative metric. The SEC value was obtained by normalizing energy consumption to the total amount of boron removed, calculated as the integral of the difference between the feed boron concentration and the effluent boron concentration during the charging phase and then multiplied by the volumetric feed flow rate. The pristine electrode showed an SEC value of 0.260 ± 0.010 kWh g-B^{-1} (Fig. 3d, red dashed line). The functionalized electrodes showed a substantial decrease in SEC values (ranging

https://doi.org/10.1038/s44221-024-00362-y

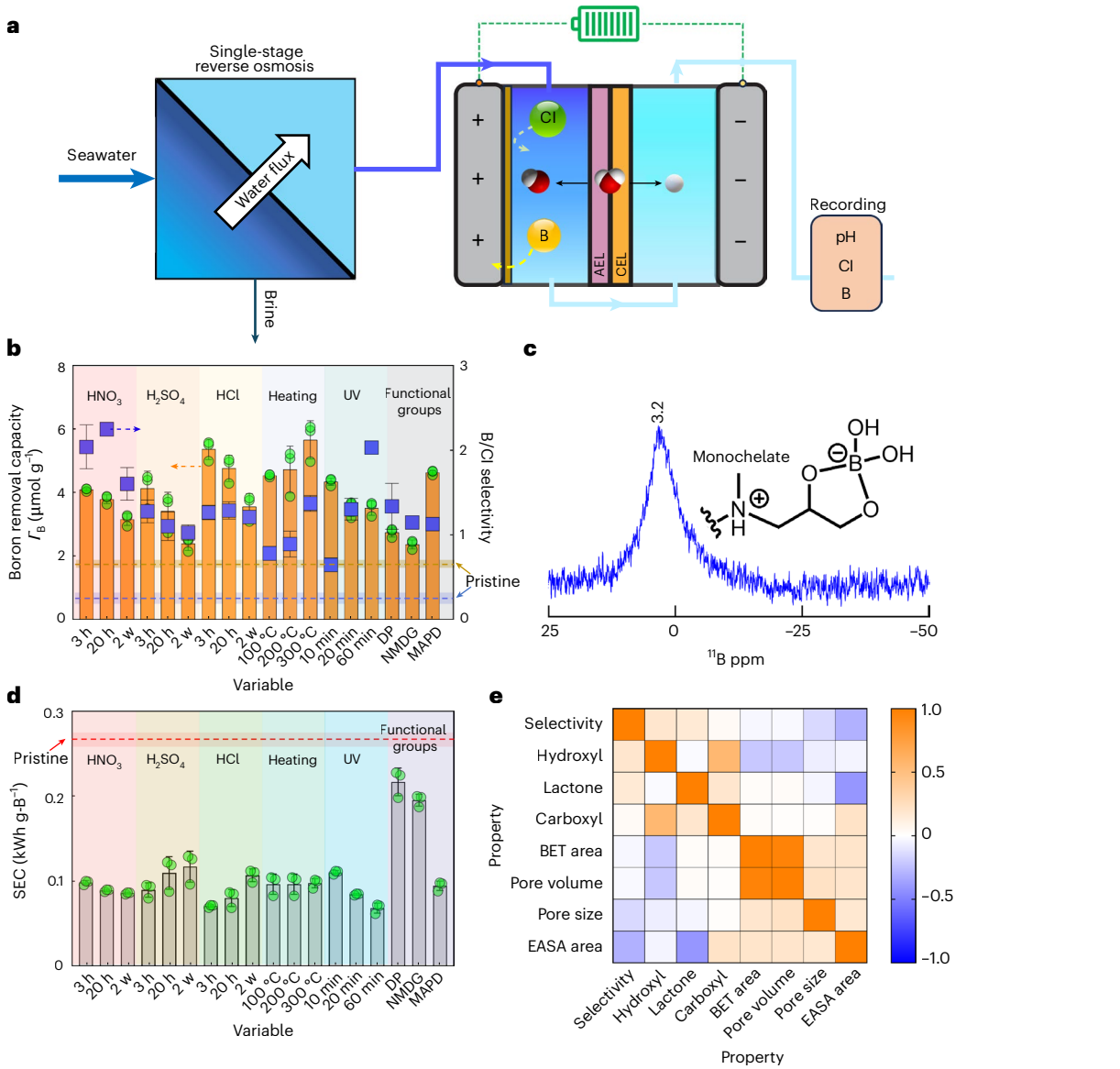

Fig. 3 | Electrode performance after chemical functionalization. a, Schematic view of electrode performance testing set-up. AEL and CEL represent anion exchange layer and cation exchange layer of the bipolar membrane, respectively. **b**, Boron removal capacity (Γ_B, orange bar) and B/Cl selectivity (blue square) of functionalized electrodes. Data are presented as mean ± standard deviation (s.d.) derived from three consecutive cycles ($n = 3$) during charging. The orange dashed line represents the mean boron removal capacity of the pristine electrode over three consecutive cycles, whereas the corresponding shaded area represents the s.d. from these cycles ($n = 3$). The blue dashed line represents the mean B/Cl selectivity of the pristine electrode over three consecutive cycles, whereas the corresponding shaded area represents the s.d. from these cycles ($n = 3$). w represents week. **c**, ^{11}B MAS NMR spectroscopy with used MAPD-functionalized electrodes. **d**, Specific energy consumption (SEC) of functionalized electrodes. Data are presented as mean ± s.d. derived from three consecutive cycles ($n = 3$) during charging. The red dashed line represents the mean SEC of the pristine electrode over three consecutive cycles, while the corresponding shaded area represents the s.d. from these cycles ($n = 3$). w represents week. **e**, Kendall rank correlation coefficients of different properties. The BPM-assisted electrosorption system was operated with a feedwater containing 5 mM NaCl and 1 mM B(OH)$_3$ at a flow rate of 3.0 ml min^{-1} in a single-pass configuration. The anode and cathode sides received identical feedwater without pH adjustment (pH 6.0 ± 0.2). Each cycle consists of applying 1.0 V for 20 minutes (charging period) followed by 0 V for 40 min (discharging period). Before collecting samples, the system was allowed to operate overnight (>12 h) to exclude the effect of pure adsorption. The determination of B/Cl selectivity (blue square in **b**) is described in Supplementary Text 2. DP, MAPD and NMDG represent dopamine, 3-methylamino-1,2-propanediol and *N*-methyl-D-glucamine, respectively.

from 0.068 ± 0.004 to 0.217 ± 0.013 kWh g-B^{-1}) after functionalization (Fig. 3d, grey bars), suggesting that the functional groups enable energy efficient boron electrosorption. Overall, the electrodes functionalized with basic oxygen-containing groups exhibited lower SEC values (ranging from 0.068 ± 0.004 to 0.117 ± 0.015 kWh g-B^{-1}) compared to those functionalized with boron-selective functional groups (ranging from 0.094 ± 0.004 to 0.217 ± 0.013 kWh g-B^{-1}). The lower SEC of electrodes functionalized with basic oxygen-containing groups is attributed to their higher boron removal capacity. This difference may also be due to more severe Faradaic reactions occurring with electrodes functionalized with boron-selective groups (MAPD, NMDG and DP)[46]. Whereas we acknowledge that these SEC values of basic oxygen-containing groups functionalized electrodes are not substantially lower than those reported (for example, 0.09 kWh g-B^{-1} for membrane-assisted electrosorption[28] and 0.14 kWh g-B^{-1} for flow-through electrosorption[27]), our functionalization methods exhibit versatility when applied to various commercial carbon cloths, which may result in substantially lower SEC values.

Hydrogen bonding governs selective boron electrosorption

To further understand the electrode property–performance relationship, we calculated the Kendall rank correlation coefficients of collected data (Fig. 3f and Supplementary Table 3). We utilized Kendall correlation due to the relatively small sample size, assuming that each pair of data is monotonically related[47]. The hydroxyl, lactone and carboxyl group densities are normalized by the corresponding electrochemically active surface areas, which are more relevant than the BET surface areas. Warm colours (orange) represent positive relationship, whereas cool colours (blue) denote negative correlation. The B/Cl selectivity shows the highest positive relationship with hydroxyl density (0.190), indicating that hydroxyl groups impact B/Cl selectivity much more than the other functional groups examined. One hypothesis is that hydroxyl groups form hydrogen bonds with borate during the electrosorption process, with hydroxyl groups acting as hydrogen bond donors and lactones as acceptors, thereby enhancing B/Cl selectivity during the electrosorption process. We note that the correlation between hydroxyl group density and B/Cl selectivity is relatively weak, which can be attributed to the influence of multiple unconsidered factors (for example, the distribution of functional groups, charging time and applied voltage) and the small sample size in our study. This aspect warrants further investigation in future studies. Negative correlations were noted with EASA (−0.307) and pore size (−0.150), possibly attributable to their impact on surface functional group loading during the functionalization process.

The mechanism underlying the selectivity of the electrosorption process for boron over chloride was further investigated using molecular dynamics (MD) simulations with slit-pore systems (Fig. 4a). Hydroxyl groups were chosen as the representative functional group for these calculations due to their prevalence on electrode surfaces and their stronger positive correlation with B/Cl selectivity compared to other functional groups. MD simulations were conducted under conditions mirroring the experimental set-up (that is, 1 V applied potential and a B/Cl concentration ratio of 1:5). The slit-pore surfaces (Fig. 4b and Supplementary Fig. 15) were functionalized with varying densities of hydroxyl groups (0, 0.38, 0.76, 1.14 and 1.71 μmol m^{-2}). The hydroxyl group density range was selected based on the BET surface areas and Boehm titration results depicted in Fig. 2. Hydroxide ions were not considered in the MD simulations due to their much lower concentration (that is, at least two orders of magnitude) compared to boron and chloride in the experiment.

Figure 4c,d illustrates that normalized boron removal performance and the corresponding B/Cl selectivity increased (from 1.00 to 1.71 and 0.85 to 2.89, respectively) with surface hydroxyl group density, consistent with the Kendall rank correlation coefficients in Fig. 3f showing a positive correlation between hydroxyl group density and B/Cl selectivity. The ion surface adsorption free energies at $\Delta\Psi = 1$ V (Fig. 4e) indicate that consistent with the boron removal capacity profile in Fig. 4c, electrosorption of $B(OH)_4^-$ ions becomes energetically more favourable with increasing hydroxyl group density. Whereas chloride adsorption is favoured on pristine carbon slit-pores, with increasing hydroxyl group density, $B(OH)_4^-$ adsorption is favoured. It is noteworthy that by solely considering electrostatic interactions, one might expect Cl^- to be preferentially adsorbed due to its smaller size and centred charge on the Cl atom, which typically results in stronger electrostatic interactions. Conversely, $B(OH)_4^-$ has a more distributed charge and is bulkier, leading to weaker electrostatic interactions. However, the observed increase in B/Cl selectivity implies that other factors beyond electrostatic interactions are important.

Further insights into the selective boron removal capacity were gained by investigating the distribution of $B(OH)_4^-$ and Cl^- ions inside the slit-pore. The number density profiles as a function of distance from slit-pore surfaces (Fig. 4f) show that two $B(OH)_4^-$ layers (Fig. 4f, solid green line) form in the slit-pore localized near walls (Fig. 4f, dashed black lines), whereas Cl^- ions exhibit a unimodal distribution at the pore centre (Fig. 4f, solid red line). An increase in the number of $B(OH)_4^-$ ions inside the pore is observed with increasing hydroxyl group density, with the majority positioned near slit-pore surfaces (Supplementary Fig. 16). Finally, the evolution of the hydrogen bond network of $B(OH)_4^-$ inside the slit-pore with increasing surface hydroxyl density was investigated. On a pristine carbon surface with no hydroxyl groups, $B(OH)_4^-$ ions form hydrogen bonds with water molecules ($H_{pristine}$). However, with the introduction of hydroxyl groups to the electrode surface, a rearrangement of hydrogen bonds occurs. Specifically, whereas the number of H_2O-$B(OH)_4^-$ hydrogen bonds slightly decreases, new OH–$B(OH)_4^-$ hydrogen bonds emerge. These findings suggest that $B(OH)_4^-$ ions display more favourable interactions with the surface in the presence of hydroxyl groups. This phenomenon contributes to an increase in boron removal capacity and enhances B/Cl selectivity.

Conclusion

Most attempts to use electrosorption for amphoteric anion (for example, boron) removal have failed to substantially improve selectivity over competing anions. Our work demonstrates two strategies for boosting the selectivity of electrodes towards boron during the electrosorption process: (1) increasing basic oxygen-containing functional groups via thermal annealing, UV irradiation and acid treatment methods and (2) incorporating boron-selective functional groups via direct surface grafting. Both strategies alter the morphology, increase surface areas and elevate surface functional group densities, thereby enhancing boron removal capacity and B/Cl selectivity. Notably, the electrode treated with 1 M HNO_3 for 20 h exhibits exceptional B/Cl selectivity of 2.25 (one order of magnitude higher than the pristine electrode) and low energy consumption.

When leveraging functional groups to improve the electrosorption of targeted contaminants, it is crucial to find the sweet spot for the contaminant–functional group interaction. This interaction should not be excessively strong, such as forming chemical bonds, as this may hinder the release of the contaminant during the discharge cycle with no voltage applied or increase the energy consumption when reverse voltage is applied in the discharge cycle. Our study reveals that electrodes functionalized with boron-selective groups (MAPD, NMDG and DP groups) form irreversible complexes with boron during electrosorption, resulting in moderate boron removal performance. On the other hand, electrodes functionalized with basic oxygen-containing groups (hydroxyl, carboxyl and lactone groups) can form hydrogen bonding with boron, which, whereas relatively weaker than complex formation, is ideal for enhancing boron selectivity as boron binding is reversible during the electrosorption process.

Overall, this study highlights the promise of functionalized electrodes in enabling BPM-assisted boron-selective electrosorption, while also providing mechanistic understanding of selective boron electrosorption. In the meantime, we acknowledge that further optimization of the process holds the key to unlocking its full potential. Engineering strategies, such as separating the BPM-assisted electrosorption process into a bipolar membrane electrodialysis process for acid/base generation and a flow-through electrosorption process, may enhance overall performance and lower the energy consumption. We note that the current cost of BPM membranes may hamper the large-scale application of the BPM-assisted boron electrosorption process[48]. However, we anticipate that advancements in BPM manufacturing methods will reduce these costs, enabling real-world application of this technology. We also envision this platform being used beyond boron removal. With the capability of our platform to induce pH variation, enable electrode functionalization and optimize operational parameters, it has the potential for highly selective removal of other contaminants and for resource recovery.

https://doi.org/10.1038/s44221-024-00362-y

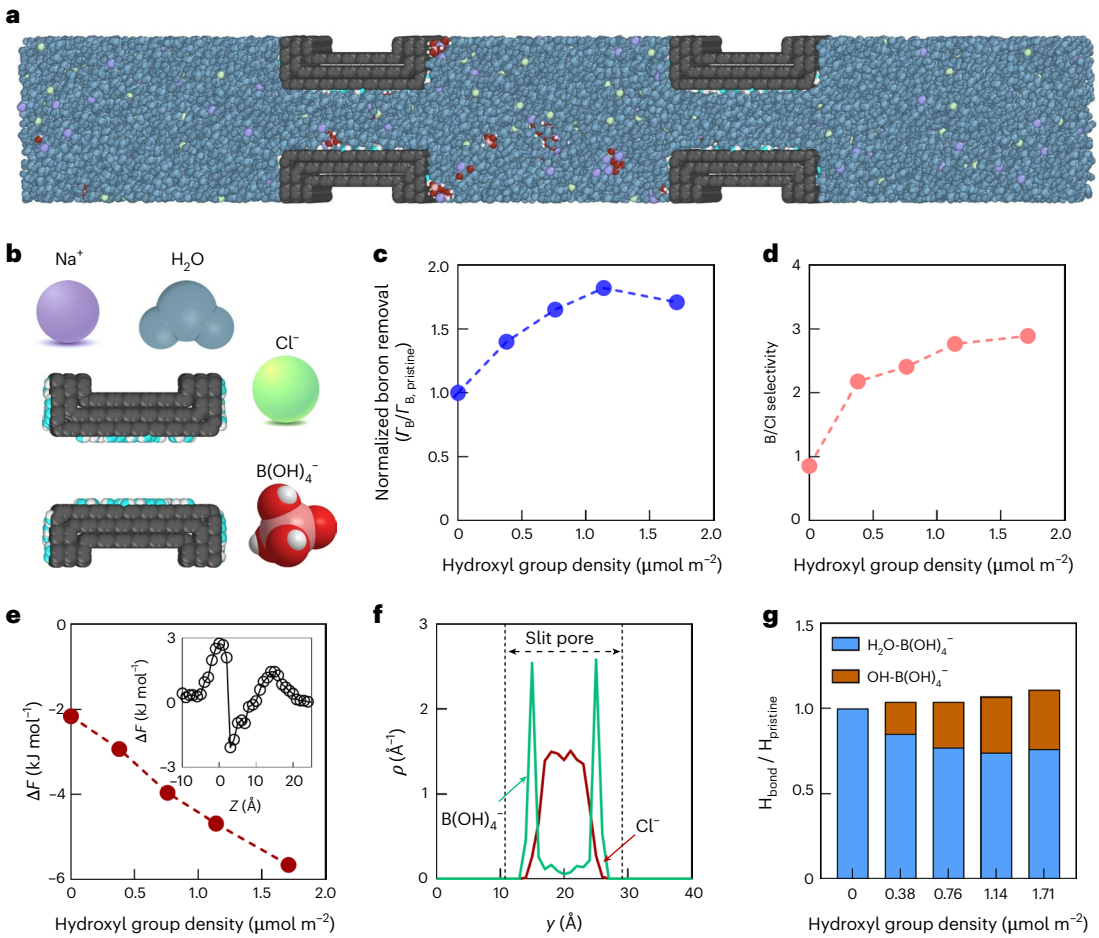

Fig. 4 | Mechanisms exploration. a, Simulated electrosorption system. **b**, Illustration of the models used in the simulations for H_2O (blue), Na^+ (purple), Cl^- (green) and $B(OH)_4^-$ (red). The slit-pore is composed of three layers of carbon atoms with its basal plane exposed. **c**, Boron removal capacity of electrodes with different hydroxyl density, normalized by the pristine electrode (that is, no hydroxyl group). **d**, $B(OH)_4^-/Cl^-$ selectivity. **e**, $B(OH)_4^-$ surface adsorption free energy as a function of surface functional group density. The inset shows the free energy profile for moving a $B(OH)_4^-$ ion in the pristine slit-pore as a function of distance from the pore entrance. ΔF represents the ion surface adsorption free energy. Z represents the distance from the pore entrance; negative values indicate being outside the pore, while positive values indicate being inside the pore. **f**, Number density profiles of $B(OH)_4^-$ and Cl^- inside the slit-pore at hydroxyl group density of 1.71 μmol m^{-2}. ρ and y represent the number density and the distance from the last layer of the slit-pore (which is unexposed), respectively. **g**, H_{bond} distribution of $B(OH)_4^-$ inside a slit-pore normalized by the number of hydrogen bonds made by $B(OH)_4^-$ inside the pristine slit-pore surface as a function of surface functional group density.

Methods

Materials

The materials and chemical reagents used in this study are listed in Supplementary Text 3.

Electrode preparation

Six types of electrode were prepared via two chemical functionalization methods. The first method involved using thermal annealing, ultraviolet irradiation and acid treatment to introduce basic oxygen-containing groups to the pristine electrode. Different thermal annealing temperatures (100–300 °C), ultraviolet exposure time (10–60 min) and acid types (H_2SO_4, HNO_3 and HCl) and treatment durations (3 h to 2 weeks) were used for electrode preparation. The second functionalization method introduced boron-selective groups (that is, DP, NMDG and MAPD) to the pristine electrode. More details can be found in Supplementary Text 1.

Electrode characterization

Boehm titration was carried out to quantitatively determine the surface functional groups on the functionalized electrodes using a pH auto titrator (Orionstar T910, Thermo-Fisher Scientific). In this method, the surface functional groups are neutralized with a base. On the basis of the pK_a of the base, the molar concentration of different functional groups can be determined. $NaHCO_3$ ($pK_a = 6.4$) reacts only with carboxylic groups, Na_2CO_3 ($pK_a = 10.3$) reacts with both carboxylic and lactonic groups and NaOH ($pK_a = 15.7$) reacts with carboxylic, lactonic, and phenolic/hydroxyl groups. The preparation of the samples and corresponding titration measurements were performed through the following steps:

1. From each functionalized electrode, ~0.1 g of sample was weighed, cut into small pieces and added to a 50 ml solution of any of the three reaction bases, that is, NaOH, $NaHCO_3$ or Na_2CO_3, each having concentration of 0.05 M.
2. Each mixture was stirred for 30 min to uniformly disperse the small electrode pieces in the medium. After this period, the stirring was stopped, and the mixture was left undisturbed for 24 h to completely neutralize the functional groups on the electrode surface.
3. After the equilibration period, the samples were filtered using a syringe filter (polyethersulfone, 0.45 μm) to remove the dispersed pieces. For the case of NaOH and $NaHCO_3$, an aliquot

of 10 ml was taken and acidified by addition of 20 ml of 0.05 M HCl. For Na_2CO_3, an aliquot of 10 ml was acidified by addition of 30 ml of 0.05 M HCl.

4. The acidified solutions were back titrated with 0.05 M NaOH using the auto titrator. The titration curve (solution pH vs volume of NaOH added) for each sample was generated and further analysed to determine the neutralization point (NaOH needed to attain neutral solution pH).
5. The following equation was used to determine the quantity of surface groups:

$$n_{CSF} = \left(\frac{n_{HCl}}{n_B}\right)[B]\,V_B - ([HCl]\,V_{HCl} - [NaOH]\,V_{NaOH})\left(\frac{V_B}{V_a}\right) \quad (1)$$

where $[B]$ is the concentration of reaction base mixed with electrode, V_B is the volume of reaction base mixed with electrode, V_a is the volume of aliquot taken from V_B, [HCl] is the concentration of HCl added to the aliquot taken from the original sample, V_{HCl} is the volume of acid added to the aliquot taken from the original sample, [NaOH] is the concentration of the titrant in the back titration, V_{NaOH} is the volume of the titrant in the back titration, $\left(\frac{n_{HCl}}{n_B}\right)$ is the molar ratio of acid to base and n_{CSF} is molar concentration of surface functional groups (mol g^{-1} of electrode)[49–51].

Details of the other characterization methods can be found in Supplementary Text 4.

Electrode performance examination

The electrode performance was tested with a custom-built bipolar membrane (BPM)-assisted electrosorption cell. Detailed structure of the BPM-assisted electrosorption cell is presented in Supplementary Fig. 10. The fabrication of the cell is detailed in Supplementary Text 5. Feedwater containing 5 mM NaCl and 1 mM $B(OH)_3$ was delivered to the cell from a 20 l polypropylene reservoir using a MasterFlex L/S peristaltic pump at a flow rate of 3.0 ml min^{-1} in single-pass mode, without recirculation. Whereas this boron concentration exceeds typical RO permeate levels, the B/Cl ratio reflects realistic conditions[10,52]. Both the anode and cathode received identical influent solution. The pH, conductivity and dissolved oxygen of the effluent from the anode side were continuously measured and recorded in 20 s intervals using in-line probes inserted into a custom-made acrylic probe holder with a cylindrical flow path. Time series effluent samples were collected by opening an in-line four-way stopcock for 20 s (1 ml samples). Before sample collection, the system underwent an overnight equilibration period, during which the same solution, without applied potentials, was fed to eliminate any pure adsorption effects. Additionally, three consecutive charging/discharging cycles were conducted before the initial sampling event. Boron removal/release capacity was determined by integrating the changes in boron concentrations with time during the charging (electrosorption) and discharging (desorption) sessions. The amounts of boron removed during charging and released during discharging closely agree (>95%, Supplementary Fig. 17) under all testing conditions.

A CH Instruments 660E potentiostat was used to regulate the applied potential throughout the experiments, with the current being recorded in 1 s intervals. The boron concentration of the collected samples was measured using the Azomethine-H colorimetric method[53,54]. Detailed information regarding the preparation of azomethine-H solution, buffer solution, boron standard solutions and its analysis is described in the Supplementary Text 6. Chloride concentrations were obtained using a Metrohm 940 Professional IC Vario ion chromatograph. All samples were collected and stored in polypropylene containers to avoid potential contamination from borosilicate glassware.

Calculation of specific energy consumption

Specific energy consumption (SEC) represents the energy consumed per unit of boron removed and serves as a crucial parameter for assessing process efficiency. Energy consumption is calculated by multiplying the applied voltage (V) by the integral of the current (I) over the charging duration (t_c), representing the total charge transferred during the process:

$$SEC = \frac{V\int_0^{t_c} I\,dt}{Q\int_0^{t_c}(C_{B,0} - C_B)\,dt} \quad (2)$$

To determine the SEC, we normalize the energy consumption by the total amount of boron removed. This is achieved by integrating the difference between the initial boron concentration in the feed ($C_{B,0}$) and the effluent boron concentration (C_B) over the charging step and then multiplying by the volumetric feed flow rate (Q). It is important to note that in our calculations, energy consumption is normalized by the mass of boron removed rather than the volume of water treated. This decision was based on the relatively small extent of boron removal achieved by our laboratory-scale system and the transient effluent condition inherent in constant voltage operation of electrosorption systems.

Molecular dynamics simulations

Slit-pore simulations. The charging simulations of the slit-pore systems were conducted in the constant potential ensemble[55] at fixed temperature T and system volume. The simulation setups are comprised of molecular models of aqueous sodium tetrahydroxyborate ($[Na]^+[B(OH)_4]^-$) and sodium chloride ($[Na]^+[Cl]^-$) solutions confined by slit-pore electrodes (Fig. 4a). TIP3P water model was used to describe water molecules[56]. The topology files and molecularly optimized geometric structures of molecules in this study were constructed using an automated topology builder[57]. The slit-pores are composed of three parallel honeycomb lattices of carbon atoms with a distance between layers at 3.38 Å. The parameters for electrode carbon atoms were adopted from Cole and Klein[58]. Harmonic bond, angle and dihedral parameters for the hydroxyl groups were taken from the OPLS-AA/L forcefield[59]. Crossed parameters were calculated by Lorentz–Berthelot mixing rules.

The distance between slit-pore surfaces was set to 18 Å. MD simulations were conducted under a constant number of particles, volume and temperature (NVT) ensemble using a time step of 1 fs and a Nose–Hoover thermostat with a relaxation time constant of 0.1 ps. The systems were constructed to target the density of the bulk aqueous solution region of the simulation setups to be equal to the respective density of the bulk solution from isothermal–isobaric ensemble simulation at 1 atm and T = 300 K. The systems were first equilibrated without applying a potential difference between the electrodes for 10 ns (that is, setting charges of the electrode atoms to zero), followed by 5 ns equilibration at $\Delta\Psi$ = 0 V in the constant potential ensemble. After equilibration, a constant potential difference of $\Delta\Psi$ = 1 V was applied between the electrodes followed by 10 ns production runs until the electrodes fully charge.

Bulk electrolyte simulation. MD simulations of the bulk aqueous solution were performed in the isothermal isobaric (NPT) ensemble at 1 atm and 300 K using a 1 fs time step. In these simulations, Nose–Hoover thermostat and barostat with relaxation time constants of 0.1 and 0.5 ps, were used, respectively. The system was first equilibrated for 1 ns, followed by a 10 ns production run.

Data availability

The data supporting the findings of this study are available within the paper and its Supplementary Information. All data files in .xlsx format are available as Supplementary Data 1–3. Source data are provided with this paper.

References

1. Mekonnen, M. M. & Hoekstra, A. Y. Four billion people facing severe water scarcity. *Sci. Adv.* **2**, e1500323 (2016).

2. Rodell, M. et al. Emerging trends in global freshwater availability. *Nature* **557**, 651–659 (2018).
3. Mauter, M. S. et al. The role of nanotechnology in tackling global water challenges. *Nat. Sustain.* **1**, 166–175 (2018).
4. Kurwadkar, S. et al. Per- and polyfluoroalkyl substances in water and wastewater: a critical review of their global occurrence and distribution. *Sci. Total Environ.* **809**, 151003 (2022).
5. Elimelech, M. & Phillip, W. A. The future of seawater desalination: energy, technology, and the environment. *Science* **333**, 712–717 (2011).
6. Gin, D. L. & Noble, R. D. Designing the next generation of chemical separation membranes. *Science* **332**, 674–676 (2011).
7. Wang, L. et al. Water transport in reverse osmosis membranes is governed by pore flow, not a solution-diffusion mechanism. *Sci. Adv.* **9**, eadf8488 (2023).
8. Patel, S. K., Biesheuvel, P. M. & Elimelech, M. Energy consumption of brackish water desalination: identifying the sweet spots for electrodialysis and reverse osmosis. *ACS ES&T Eng.* **1**, 851–864 (2021).
9. Wang, L., Violet, C., DuChanois, R. M. & Elimelech, M. Derivation of the theoretical minimum energy of separation of desalination processes. *J. Chem. Edu.* **97**, 4361–4369 (2020).
10. Greenlee, L. F., Lawler, D. F., Freeman, B. D., Marrot, B. & Moulin, P. Reverse osmosis desalination: water sources, technology, and today's challenges. *Water Res.* **43**, 2317–2348 (2009).
11. Patel, S. K., Pan, W., Shin, Y.-U., Kamcev, J. & Elimelech, M. Electrosorption integrated with bipolar membrane water dissociation: a coupled approach to chemical-free boron removal. *Environ. Sci. Technol.* **57**, 4578–4590 (2023).
12. *Boron in Drinking-Water: Background Document for Development of WHO Guidelines for Drinking-Water Quality* (World Health Organization, 2009).
13. Weinthal, E., Parag, Y., Vengosh, A., Muti, A. & Kloppmann, W. The EU drinking water directive: the boron standard and scientific uncertainty. *Eur. Environ.* **15**, 1–12 (2005).
14. DeLeo, P. C., Stuard, S. B., Kinsky, O., Thiffault, C. & Baisch, B. Assessment of consumer exposure to boron in cleaning products: a case study of Canada. *Crit. Rev. Toxicol.* **51**, 359–371 (2021).
15. *Drinking Water Health Advisory for Boron* (US EPA, 2008); https://www.epa.gov/sites/default/files/2014-09/documents/drinking_water_health_advisory_for_boron.pdf
16. Hilal, N., Kim, G. J. & Somerfield, C. Boron removal from saline water: a comprehensive review. *Desalination* **273**, 23–35 (2011).
17. Lokiec, F. & Kronenberg, G. South Israel 100 million m^3/y seawater desalination facility: build, operate and transfer (BOT) project. *Desalination* **156**, 29–37 (2003).
18. Rybar, S., Boda, R. & Bartels, C. Split partial second pass design for SWRO plants. *Desalin. Water Treat.* **13**, 186–194 (2010).
19. Chillón Arias, M. F., Valero i Bru, L., Prats Rico, D. & Varó Galvañ, P. Approximate cost of the elimination of boron in desalinated water by reverse osmosis and ion exchange resins. *Desalination* **273**, 421–427 (2011).
20. Güler, E., Kaya, C., Kabay, N. & Arda, M. Boron removal from seawater: state-of-the-art review. *Desalination* **356**, 85–93 (2015).
21. Suss, M. E. et al. Water desalination via capacitive deionization: what is it and what can we expect from it? *Energy Environ. Sci.* **8**, 2296–2319 (2015).
22. Alkhadra, M. A. et al. Electrochemical methods for water purification, ion separations, and energy conversion. *Chem. Rev.* **122**, 13547–13635 (2022).
23. Oren, Y. Capacitive deionization (CDI) for desalination and water treatment—past, present and future (a review). *Desalination* **228**, 10–29 (2008).
24. Qin, M. et al. Comparison of energy consumption in desalination by capacitive deionization and reverse osmosis. *Desalination* **455**, 100–114 (2019).
25. Patel, S. K., Qin, M., Walker, W. S. & Elimelech, M. Energy efficiency of electro-driven brackish water desalination: electrodialysis significantly outperforms membrane capacitive deionization. *Environ. Sci. Technol.* **54**, 3663–3677 (2020).
26. Shocron, A. N. et al. Electrochemical removal of amphoteric ions. *Proc. Natl Acad. Sci.* **118**, e2108240118 (2021).
27. Shocron, A. N., Uwayid, R., Guyes, E. N., Dykstra, J. E. & Suss, M. E. Order-of-magnitude enhancement in boron removal by membrane-free capacitive deionization. *Chem. Eng. J.* **466**, 142722 (2023).
28. Sun, J., Zhang, C., Song, Z. & Waite, T. D. Boron removal from reverse osmosis permeate using an electrosorption process: feasibility, kinetics, and mechanism. *Environ. Sci. Technol.* **56**, 10391–10401 (2022).
29. Gamaethiralalage, J. G. et al. Recent advances in ion selectivity with capacitive deionization. *Energy Environ. Sci.* **14**, 1095–1120 (2021).
30. DeFrancesco H., Dudley J. & Coca A. in *Boron Reagents in Synthesis* Ch. 1 (ed. Coca, A.) (American Chemical Society, 2016).
31. Guan, Z., Lv, J., Bai, P. & Guo, X. Boron removal from aqueous solutions by adsorption—a review. *Desalination* **383**, 29–37 (2016).
32. Kamcev, J. et al. Functionalized porous aromatic frameworks as high-performance adsorbents for the rapid removal of boric acid from water. *Adv. Mater.* **31**, 1808027 (2019).
33. Uliana, A. A. et al. Ion-capture electrodialysis using multifunctional adsorptive membranes. *Science* **372**, 296–299 (2021).
34. Polovina, M., Babić, B., Kaluderović, B. & Dekanski, A. Surface characterization of oxidized activated carbon cloth. *Carbon* **35**, 1047–1052 (1997).
35. Cheng, N. et al. Acidically oxidized carbon cloth: a novel metal-free oxygen evolution electrode with high catalytic activity. *Chem. Commun.* **51**, 1616–1619 (2015).
36. Bard A. J., Faulkner L. R. & White H. S. *Electrochemical Methods: Fundamentals and Applications* (Wiley, 2022).
37. Trasatti, S. & Petrii, O. Real surface area measurements in electrochemistry. *Pure Appl. Chem.* **63**, 711–734 (1991).
38. Zhang, Z. & Flaherty, D. W. Modified potentiometric titration method to distinguish and quantify oxygenated functional groups on carbon materials by pK_a and chemical reactivity. *Carbon* **166**, 436–445 (2020).
39. Petrovic, B., Gorbounov, M. & Masoudi Soltani, S. Impact of surface functional groups and their introduction methods on the mechanisms of CO_2 adsorption on porous carbonaceous adsorbents. *Carbon Capture Sci. Technol.* **3**, 100045 (2022).
40. Boehm, H. P. Some aspects of the surface chemistry of carbon blacks and other carbons. *Carbon* **32**, 759–769 (1994).
41. Bhagyaraj, S., Al-Ghouti, M. A., Kasak, P. & Krupa, I. An updated review on boron removal from water through adsorption processes. *Emergent Mater.* **4**, 1167–1186 (2021).
42. Soga, T. & Ross, G. A. Simultaneous determination of inorganic anions, organic acids, amino acids and carbohydrates by capillary electrophoresis. *J. Chromatogr. A* **837**, 231–239 (1999).
43. Lin, J.-Y., Mahasti, N. N. N. & Huang, Y.-H. Recent advances in adsorption and coagulation for boron removal from wastewater: a comprehensive review. *J. Hazard. Mater.* **407**, 124401 (2021).
44. Yoshimura, K., Miyazaki, Y., Ota, F., Matsuoka, S. & Sakashita, H. Complexation of boric acid with the *N*-methyl-D-glucamine group in solution and in crosslinked polymer. *J. Chem. Soc., Faraday Trans.* **94**, 683–689 (1998).
45. Manjunatha Reddy, G., Gerbec, J. A., Shimizu, F. & Chmelka, B. F. Nanoscale surface compositions and structures influence boron adsorption properties of anion exchange resins. *Langmuir* **35**, 15661–15673 (2019).

46. Kang, J. S. et al. Surface electrochemistry of carbon electrodes and Faradaic reactions in capacitive deionization. *Environ. Sci. Technol.* **56**, 12602–12612 (2022).
47. Kotz, S., Balakrishnan, N., Read, C. B., Vidakovic, B. & Johnson, N. L. *Encyclopedia of Statistical Sciences* Vol. 1 (Wiley, 2005).
48. Wang, Y., Huang, C. & Xu, T. Which is more competitive for production of organic acids, ion-exchange or electrodialysis with bipolar membranes? *J. Membr. Sci.* **374**, 150–156 (2011).
49. Xing, Y., Dementev, N. & Borguet, E. Chemical labeling for quantitative characterization of surface chemistry. *Curr. Opin. Solid State Mater. Sci.* **11**, 86–91 (2007).
50. Goertzen, S. L., Thériault, K. D., Oickle, A. M., Tarasuk, A. C. & Andreas, H. A. Standardization of the Boehm titration. Part I. CO_2 expulsion and endpoint determination. *Carbon* **48**, 1252–1261 (2010).
51. Sneh, O. & George, S. M. Thermal stability of hydroxyl groups on a well-defined silica surface. *J. Phys. Chem.* **99**, 4639–4647 (1995).
52. Lim, Y. J., Goh, K., Kurihara, M. & Wang, R. Seawater desalination by reverse osmosis: current development and future challenges in membrane fabrication–a review. *J. Membr. Sci.* **629**, 119292 (2021).
53. Spencer, R. R. & Erdmann, D. E. Azomethine H colorimetric method for determining dissolved boron in water. *Environ. Sci. Technol.* **13**, 954–956 (1979).
54. López, F., Giménez, E. & Hernández, F. Analytical study on the determination of boron in environmental water samples. *Fresenius J. Anal. Chem.* **346**, 984–987 (1993).
55. Siepmann, J. I. & Sprik, M. Influence of surface topology and electrostatic potential on water/electrode systems. *J. Chem. Phys.* **102**, 511–524 (1995).
56. Price, D. J. & Brooks, C. L. III A modified TIP3P water potential for simulation with Ewald summation. *J. Chem. Phys.* **121**, 10096–10103 (2004).
57. Malde, A. K. et al. An automated force field topology builder (ATB) and repository: version 1.0. *J. Chem. Theory Comput.* **7**, 4026–4037 (2011).
58. Cole, M. W. & Klein, J. R. The interaction between noble gases and the basal plane surface of graphite. *Surf. Sci.* **124**, 547–554 (1983).
59. Kaminski, G. A., Friesner, R. A., Tirado-Rives, J. & Jorgensen, W. L. Evaluation and reparametrization of the OPLS-AA force field for proteins via comparison with accurate quantum chemical calculations on peptides. *J. Phys. Chem. B* **105**, 6474–6487 (2001).

Acknowledgements

This work was supported by the National Alliance for Water Innovation (NAWI), funded by the US Department of Energy, Office of Energy Efficiency and Renewable Energy (EERE), Advanced Manufacturing Office, under Funding Opportunity Announcement Number DE-FOA-0001905, and by the US National Science Foundation (NSF) and US-Israel Binational Science Foundation (BSF) under award number CBET-2001219. We thank Y. Duan from the Department of Chemical and Environmental Engineering at Yale University for technical assistance with conducting the electrochemically active surface area measurement.

Author contributions

W.P., D.R., J.K. and M.E. conceptualized and designed the study. W.P., D.R. and E.A., conducted experimental research. B.U. and A.H.-A. performed computational research. W.P., D.R., B.U., S.K.P. and A.I. performed data analysis and visualization. J.K. and M.E. supervised the study. W.P., D.R., B.U., J.K. and M.E. wrote the manuscript, with all authors contributing to manuscript editing.

Competing interests

The authors declare no competing interests.

Additional information

Supplementary information The online version contains supplementary material available at https://doi.org/10.1038/s44221-024-00362-y.

Correspondence and requests for materials should be addressed to Jovan Kamcev or Menachem Elimelech.

Peer review information *Nature Water* thanks Chia-Hung Hou and the other, anonymous, reviewer(s) for their contribution to the peer review of this work.